Journal of The Electrochemical Society, **154** (4) D230-D240 (2007)
0013-4651/2007/154(4)/D230/11/$20.00 © The Electrochemical Society

Effect of Additives on Shape Evolution during Electrodeposition

I. Multiscale Simulation with Dynamically Coupled Kinetic Monte Carlo and Moving-Boundry Finite-Volume Codes

Xiaohai Li, Timothy O. Drews, Effendi Rusli, Feng Xue, Yuan He, Richard Braatz,* and Richard Alkire,z**

Department of Chemical and Biomolecular Engineering, University of Illinois, Urbana, Illinois 61801, USA

A multiscale simulation model was developed to simulate shape evolution during copper electrodeposition in the presence of additives. The model dynamically coupled a kinetic Monte Carlo (KMC) model (for surface chemistry and roughness evolution) with a finite volume (FV) model (for transport and chemical reactions in the electrolyte) and a level-set code (for tracking macroscopic movement of the metal/electrolyte interface). The KMC code was coarse-grained and used a multisite mesoparticle approach to account for the adsorption of large molecules. A multilevel grid approach was used to achieve numerical efficiency and accurate interface tracking. The model was demonstrated for an application involving in-fill of two-dimensional trenches by copper electrodeposition with additives [bis(3-sulfopropyl)disulfide], polyethylene glycol, chloride, and l-(2-hydroxyethyl)-2-imidazolidinethione. Demonstration calculations were carried out with use of initial estimates for the physicochemical parameters associated with a proposed reaction mechanism. The approach was found to be feasible for computing stable, dynamic behavior during macroscopic shape evolution over extended periods of time while simultaneously tracking microscopic roughness evolution associated with nearly molecular scale events at the surface. Numerical results include predictions of the surface concentration distributions as a function of time and distance for each reactant, product, and intermediate species associated with the proposed reaction mechanism.
 [DOI: 10.1149/1.2434686]

Manuscript submitted July 18, 2006; revised manuscript received November 27, 2006. Available electronically February 15, 2007.

The electrodeposition of metal represents a longstanding technology which is invariably carried out with use of solution additives. Such additives function at the molecular scale and influence microscopic as well as macroscopic outcomes such as the structure and properties of the deposit, growth morphology, and net final shape. Traditional engineering design methods for electrodeposition applications use mathematical models based on macroscopic reaction/transport phenomena which encounter difficulty in formulating boundary conditions with sufficient detail and chemical complexity to capture the subtle aspects of most additive systems. Numerical complications also arise, since additive-based electrodeposition processes involve phenomena that are simultaneously important over nine orders of magnitude in time and length scales.[1-4] Moreover, fundamental understanding of additive behavior at the molecular scale has advanced steadily with the recent development of many novel experimental techniques for surface characterization and imaging. Also, recent advances in high-performance computing have made possible substantial improvement in the ability to simulate small-scale stochastic processes, as well as the use of computational methods to extract information from simulations for use in decision making and design. In this work, a multiscale numerical method for the simulation of shape evolution in the presence of additives is developed and verified. The technological application selected for demonstrating the method is the electrodeposition of on-chip copper interconnects, where shape evolution during infill of small recesses depends critically on additive behavior.[5]

Most mathematical models of electrodeposition with additives are based on continuum models: usually a convection-diffusion model to describe solution-phase transport phenomena, and mean-field rate equations to account for surface chemistry.[6-10] Such continuum methods have a blind spot in the small-scale region where product quality is determined by molecular behavior at the surface.[1] To resolve this shortcoming, Pricer et al.[11,12] coupled a kinetic Monte Carlo (KMC) code with a one-dimensional (1D) continuum diffusion code to simulate copper electrodeposition in the presence of a hypothetical blocking additive. Their approach showed promise for the task of developing multiscale models of copper electrodeposition and for testing various proposed reaction mechanisms, as well as for engineering design.

Multiscale simulations have been used to simulate the deposition of thin films for various applications. Cale and co-workers[13] demonstrated an integrated multiscale process simulation framework, applying it to a simple copper electrodeposition into trenches without additives. Lam and Vlachos[14] used a coupled KMC-continuum code to simulate growth mode transitions that occur during physical vapor deposition of thin films. Hansen and co-workers[15] created a multiscale simulation model in which data obtained from molecular dynamics simulations were incorporated into a level-set model of the growing metal film.

The purpose of the present series of investigations is to develop new procedures for extracting information about a complex additive mechanism from experimental data, using that information, along with multiscale numerical methods, to simulate the effect of additives on macroscopic shape evolution. The interconnect application was selected for application of the multiscale approach because it shares common features with a wide range of applications where improved engineering procedures are needed: (*i*) detailed mechanistic information is uncertain although multiple reasonable qualitative hypotheses of behavior are available; (*ii*) critical events are difficult to observe directly by experiment, with the consequence that inferences from indirect measurements (often carried out at different scales) are used; and (*iii*) the problem is multiscale and multiphenomenal in nature, spanning from molecular details of surface chemistry and structure formation to macroscopic aspects of transport processes and reactor conditions. An integrated approach is therefore needed to link experimental data, theory, and stochastic simulations at the molecular scale, with the ability to predict accurate macroscopic outcomes with known error bars that are essential for engineering design, optimization, and control.

In this paper, stochastic- and continuum-scale models of electrodeposition phenomena are formulated and dynamically linked to compose a multiscale numerical model. The model was tested numerically with use of a set of initial estimates for the system parameters associated with in-fill of small trenches with copper in order to evaluate the feasibility of computing stable, dynamic behavior. In subsequent publications we will report on a high-throughput experimental technique used for obtaining a large set of surface roughness evolution and other electrochemical data, which were analyzed with

* Electrochemical Society Active Member.
** Electrochemical Society Fellow.
z E-mail: r-alkire@uiuc.edu

use of the multiscale model of the present work to estimate values of the most sensitive parameters of the multiscale numerical model. In subsequent publications we will also report additional experimental data on macroscopic shape evolution during trench infill in the presence of various additive compositions and compare data with numerical simulations.

Components of the Multiscale Simulation Model

Kinetic Monte Carlo code.— A solid-on-solid KMC model was formulated with the (2 + 1)D approach, where the "2D" refers to lattice sites arranged in a surface and the "+1D" refers to the height above the surface. The model was formulated to include typical phenomena that take place on the metal surface during electrodeposition, including adsorption, desorption, surface diffusion, and surface reactions. One particular hypothesis for the chemical and electrochemical reaction mechanisms was explored. The KMC code follows the BKL algorithm[16] (see Appendix A for details). For a particular mechanism there are N lattice sites that can possibly undergo M transition events. Each of the M transition events has an associated rate, r_j. Once the rates of the events are calculated, a list of transition probabilities is constructed in terms of the rates

$$W_s = \frac{n_s r_s}{\sum_j n_j r_j} \quad [1]$$

where W_s is the probability of a transition event s occurring, and n_j is the number of lattice sites out of N that are capable of undergoing transition event j with a rate r_j.[17,18] Then a particular type of event is chosen according to the above transition probability. Finally, one site among all the possible lattice sites is randomly selected to execute the chosen event. The time is increased by

$$\tau = -\frac{1}{\sum_j n_j r_j} \quad [2]$$

where $U \in (0,1)$ is a random number with uniform distribution. This algorithm is sometimes referred to as a rejection-free method and is more efficient that the null-event algorithm implemented in Ref. 11 and 12. Furthermore, to reduce the computational load while still keeping enough spatial resolution to match that of the experimental data, the KMC model was coarse-grained to form mesoparticles.[19-23] Each mesoparticle in the (2 + 1)D KMC simulation code contains a group of molecules at the same vertical position. The coarse-grained KMC approach made it possible to simulate the evolution of surface roughness at the same length scale as the experimental measurements.[24]

If all mesoparticles were the same size, then their size would need to be large enough to contain the largest molecules in the electrochemical system [e.g., poly(ethylene glycol) (PEG) in the additive system considered below], which would result in low spatial resolution. To account correctly for the surface blocking effect of large molecules while attaining a high spatial resolution, the KMC code was formulated so that mesoparticles of large molecular species were allowed to occupy more than one surface site. Such a mesoparticle is called a "multisite mesoparticle." The coding for such mesoparticles was implemented by introducing a special pseudospecies on the surface (called a "blocker"), for which no surface reactions are associated. When a large molecule is adsorbed on the surface, the KMC code fills the surrounding sites of the newly created mesoparticle with $(m - 1)$ blockers, in which m is the total number of surface sites that such a multisite mesoparticle should occupy. The blockers are only allowed to cover the same types of surface species that the multisite mesoparticle is allowed to deposit on. The blockers that belong to the same multisite mesoparticle may not be contiguous and may spread out on the entire KMC domain. This approach ensures that the surface coverage of multisite mesoparticles is consistent with the assumed molecular structure on the surface.

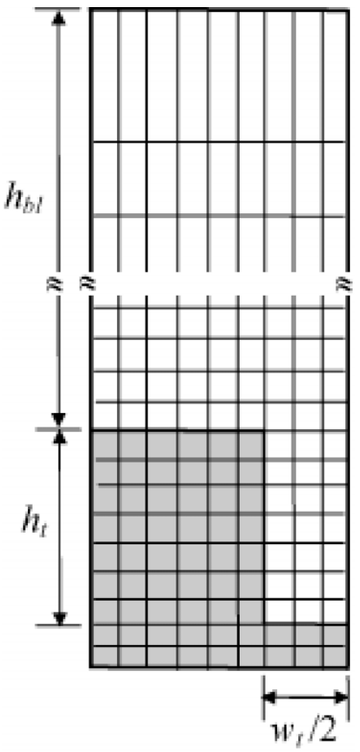

Figure 1. Schematic drawing of the initial arrangement of a trench prior to shape evolution (not to scale): w_t is the width of the trench, h_t is the depth of the trench, and h_{bl} is the thickness of the external diffusion layer. Owing to symmetry, only the left half of the trench was used in FV computations. The gray area is metal, the white area is electrolyte solution. The trench is embedded in a rectangular domain and a nonuniform Cartesian grid is used.

FV code.— A 2D FV code was developed to simulate the transport phenomena and homogeneous chemical reactions in the electrolyte. Figure 1 is a schematic diagram of the simulation domain. Taking advantage of symmetry, only the left half of the domain was used. A dilute solution model[25] was applied and the transport parameters were assumed to be independent of concentration. Thus, the mass balance on each species is given by

$$\frac{\partial C_i}{\partial t} = D_i \nabla^2 C_i + z_i F u_i \bar{\nabla} \cdot (C_i \bar{\nabla} \Phi) + A_i \quad [3]$$

where A_i is production rate of species i due to homogeneous reactions in the bulk solution. Convection has been shown to be not important within the trench at submicrometer length scales.[26] The boundary conditions on the top bulk boundary are

$$C_i = C_i^{\infty} \quad [4]$$

$$\Phi = \Phi^{\infty} \quad [5]$$

On the nonactive boundaries, the boundary conditions are

$$\bar{\mathbf{N}}_i \cdot \bar{\mathbf{n}} = 0 \quad [6]$$

where $\bar{\mathbf{n}}$ is the normal direction and $\bar{\mathbf{N}}_i$ is the flux of species i

$$\bar{\mathbf{N}}_i = D_i \bar{\nabla} C_i + z_i F u_i C_i \bar{\nabla} \Phi \quad [7]$$

On the active boundaries, the boundary conditions are

$$\bar{\mathbf{N}}_i \cdot \bar{\mathbf{n}} = J_i \quad [8]$$

where J_i is the flux of species i passed from the KMC simulation code. Finally the electroneutrality constraint

$$\sum_i z_i C_i = 0 \quad [9]$$

is applied. The above equations form a system of coupled nonlinear partial differential equations and algebraic equations (PDAEs). The numerical method of lines (NMOL)[27] was used to solve this system, an approach which may be expanded to the more general case involving convection. Spatial derivatives are approximated by the second-order finite-volume (FV) method,[28] which writes Eq. 3 in integral form

$$\int_V \frac{\partial C_i}{\partial t} dV = \int_V (\bar{\nabla} \cdot (D_i \bar{\nabla} C_i) + \bar{\nabla} \cdot (z_i F u_i C_i \bar{\nabla} \Phi) + A_i) dV \quad [10]$$

where V is the cell volume. Application of Green's theorem gives

$$\int_V \frac{\partial C_i}{\partial t} dV = \int_{\partial V} (D_i \bar{\nabla} C_i + z_i F u_i C_i \bar{\nabla} \Phi) \cdot \bar{\mathbf{n}} dS + \int_V A_i dV \quad [11]$$

where dV is the surface of the cell volume. With $\tilde{C}_i$ defined as the cell-averaged concentration and $\tilde{A}_i$ as the cell-averaged production rate

$$\frac{\partial \tilde{C}_i}{\partial t} = \frac{1}{V} \int_{\partial V} (D_i \bar{\nabla} C_i + z_i F u_i C_i \bar{\nabla} \Phi) \cdot \bar{\mathbf{n}} dS + \tilde{A}_i \quad [12]$$

The gradients are replaced by second-order approximations and the resulting system forms a set of mixed index-1 and index-2 differential algebraic equations (DAEs). The stiff DAE system was solved by DASPK by using the backward differentiation formula (BDF) method.[29] During this procedure the solution of a large linear system was required, which was accomplished by either a direct banded method or a preconditioned generalized minimum residual (GMRES) method, depending on which method was faster.

Level-set code.— The level-set method (LSM) was used to track the motion of the metal/electrolyte interface. The LSM is a highly robust and accurate method for tracking interfaces moving under complex motions.[30] It can easily handle sharp corners and topological changes, such as interface splitting and merging. In the LSM, a time-dependent level-set function, ϕ, is defined over the entire region. At any time, the interface is given by the zero level set (i.e., $\phi = 0$). Here, $\phi < 0$ and $\phi > 0$ mark the domain of copper and electrolyte, respectively. The level-set equation describing the interface evolution is

$$\phi_t + v|\bar{\nabla} \phi| = 0 \quad [13]$$

where v is the speed of interface in its normal direction. In the LSM, v is defined not only on the zero level set, but on all level sets throughout the computational domain. On the zero level set, v is naturally defined by the underlying physics. For other v, the fast marching method (FMM) is used to solve

$$\bar{\nabla} \phi^{\text{temp}} \cdot \bar{\nabla} v_{\text{ext}} = 0 \quad [14]$$

where v_{ext} is the extension velocity. By use of the extension velocity, one can avoid reinitialization, which improves efficiency and accuracy. With use of the FMM, the level-set equation can be written

$$\phi_t + v_{\text{ext}}|\bar{\nabla} \phi| = 0 \quad [15]$$

A second-order method was used for solving Eq. 14. For the solution of the level set Eq. 15, a second-order total variation nonincreasing Runge–Kutta scheme was used for the time derivative, and a second-order upwind scheme mimicking a high-order essentially nonoscillatory scheme was used for spatial discretization.[28]

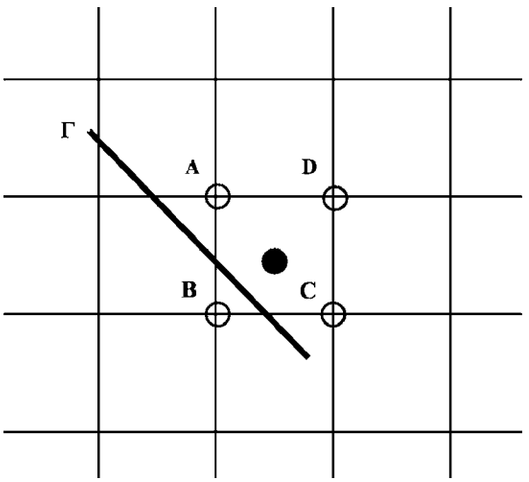

Figure 2. The staggered grid used in coupling the FV code with the level-set code. The line Γ represents the position of the metal/electrolyte interface. The cell-averaged concentrations and potential are stored at the nodes marked with (●), but values of level-set functions are stored at the nodes marked with (○).

Multilevel coupling of the FV code with the level-set code.— The FV code and the level-set code were coupled to form the moving-boundary (MB) continuum code for the simulation of the transport phenomena with a moving metal/electrolyte interface. More specifically, the MB problem was converted into a series of fixed boundary problems, i.e., at each iteration, the level-set code provides a fixed boundary for the FV code.

The whole simulation domain is embedded in a fixed nonuniform Cartesian grid (see Fig. 1), so there is no cost of mesh generation compared to other unstructured mesh-based methods. The grid is nonuniform to take into account that the thickness of the external mass-transfer diffusion layer is much larger than the size of the trench (i.e., $h_{bl} \gg h_t$). Figure 2 shows a control volume. A staggered grid is used where concentrations and potential are stored at the center of a control volume, while level-set values are stored at the vertices of the control volume. In this way the intersection of the metal/electrolyte interface and control volume can be easily obtained from the level-set values at the vertexes with the assumption that the interface is linear piecewise within a control volume.

The FV code runs more slowly than the level-set code over the same grid. Therefore a fine grid was adopted for the level-set code and a coarse grid for the FV code. The only level-set values sent to the FV code were those that corresponded to the coarse grid level. It was found during the course of this work that the multilevel grid method sped up the simulation significantly and also made the tracking of the metal/electrolyte interface more accurate. A fine grid for the level-set code also enables us to express the metal/electrolyte interface within a control volume by a high-order approximation.[31]

Coupling the MB continuum code with the KMC code.— Figure 3 illustrates schematically how the MB continuum simulation code was linked to a "necklace" of KMC domains along the trench wall, similar to the gap-tooth method of Gear et al.[32] The coupled simulation follows a "master-worker" MPI computational scheme illustrated in Fig. 4: the MB continuum code is the master code and the KMC codes are the workers. Each KMC code simulates the evolution of local surface shape and morphology at selected locations on the trench. Considering that scientific studies are traditionally carried out at constant potential while industrial operations generally use constant current, we performed constant current simulations by incorporating a feedforward-feedback controller in the simulation code (see Appendix B).

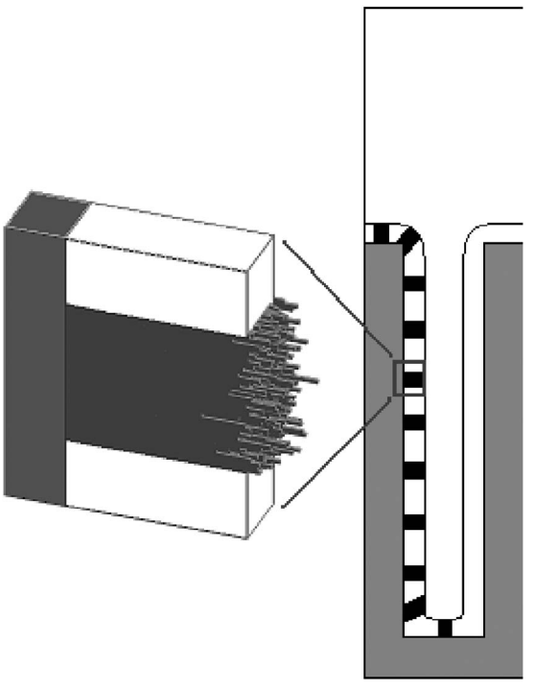

Figure 3. Right: The stripes in the copper deposit denote the location of ten individual KMC domains along the wall of a trench. Left: The zoom-in image of one of the domains illustrates the distinction between the KMC surface morphology and the surface represented in the MB continuum code.

The locations where the KMC codes were coupled were chosen to optimally reduce the interaction between successive KMC simulations, while still providing a sufficient number of points to establish the profile of macroscopic properties on the surface. The macroscopic profile serves as the boundary conditions for the continuum code in the next iteration. Because the number of KMC simulations is less than the number of nodes at the interface in the continuum code, the KMC flux values are interpolated to supply continuous flux values along the moving boundary. Conversely, the concentrations and potential from the continuum code are interpolated to get the values at the KMC locations.

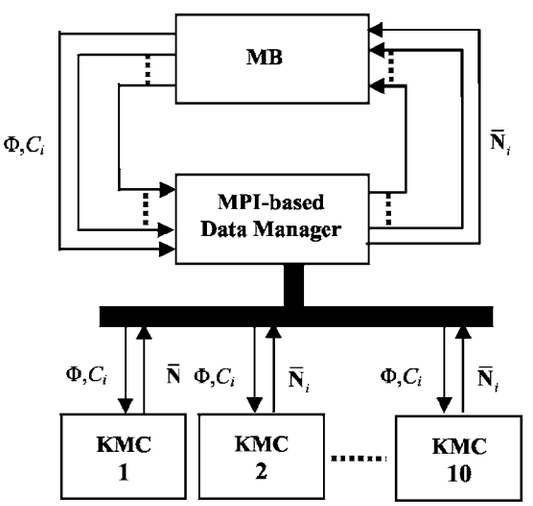

Figure 4. Information flows for the dynamically coupled multiscale simulation which uses MPI and the "master-worker" approach. The MB code is the master code and the KMC cells are the workers. The MB code sends local values of potential and species concentrations to each KMC cell. The KMC cells send local values of flux to the MB code.

Figure 4 illustrates how the information passing between the dynamically coupled codes is managed with the message passing interface (MPI) specification, which is widely used for solving significant scientific and engineering problems on parallel computers.[33] For the application at hand,[31] the coupled simulation begins with the creation of a directory tree, which holds the individual outputs from the KMC instances and continuum code during a simulation. Both the KMC and continuum codes are then launched and initiated. If the simulation is restarted from an unfinished previous run (e.g., due to the supercomputer batch job run-time limit), both surface and bulk concentrations of the species, the fluxes at the metal/electrolyte interface, and the current metal/electrolyte interface location are read into the code. Each KMC code runs for one iteration to compute the local average of species fluxes and sends the values to the continuum code via an MPI data manager (see Fig. 4). The data manager interpolates the fluxes given by the individual KMC codes and creates a new continuous flux boundary condition. Then the continuum code sends back all the local species concentrations and potential at the locations of the liquid-solid boundary where the KMC codes are positioned. The KMC codes then proceed to the next iteration. This sequence is repeated until the specified length of deposition time has elapsed. The output files store all the simulation status information that belongs to the individual KMC and the continuum codes, so that a new run can be launched from the current directory to continue on the simulation when needed.

A dynamic mechanism was used in the simulation for the initial placement of KMC simulation domains along the wall of the trench according to a predefined mesh resolution. During the simulation, the KMC simulation domains move in the normal direction of the local metal/electrolyte interface. The KMC simulation domain was removed if it becomes entrapped in a macroscopic void in the deposit.

Reaction mechanism for additive-based electrodeposition.— A hypothesis for an additive mechanism for copper electrodeposition from acid sulfate electrolyte was formulated for testing the feasibility of the simulation method. This section presents the hypothesis but defers discussion of evidence in support of the mechanism to Part II and elsewhere.[34,35] In addition, this section describes how initial estimates were made for the parameters of the hypothetical reaction mechanism; in Part II the initial estimates are used as starting points for a more detailed sensitivity analysis and parameter estimation procedure.

To address additive effects during trench infill for on-chip copper interconnects, the acid–copper sulfate system was selected: H_2SO_4 and $CuSO_4$ with chloride (as HCl), PEG, Mw 3400), [bis(3-sulfopropyl)disulfide (SPS)] and l-(2-hydroxyethyl)-2-imidazolidinethione (HIT). The hypothetical reaction mechanism summarized in Table I includes 15 surface actions (implemented in the KMC code) and three homogeneous equilibrium reactions (implemented in the FV code). The mechanism includes 12 species in the solution phase, and five species that are confined to the surface, and of these only the Cu atoms are allowed to move by surface diffusion.

Most of the reaction and transport parameters associated with the proposed mechanism in Table I are not available or were measured under different experimental conditions than used in the present work. Table I provides physical property data along with initial values for kinetic parameters which were estimated by a procedure summarized below and in detail elsewhere.[35] The initial estimates were based on chronoamperometry data collected with a flat rotating disk electrode (RDE), a simple numerical model (Appendix A in Ref. 28), and informed judgment based on knowledge of the literature.[35] The numerical model was a transient one-dimensional (1D) model that included diffusion, migration, and homogeneous

Table I. Species and reactions in copper electrodeposition.

a. Electrochemical and chemical reactions on surface.[a]

j	Surface reactions in KMC code	Rate constant k_j	α_j	E_j^0 (V)
1	$Cu^{2+}_{aq} + e^- \rightarrow Cu^+_{aq}$	1.11×10^2 (L/mol s)	0.5	−0.5
2	$Cu^+_{aq} + e^- \rightarrow Cu_s$	1.29×10^1 (L/mol s)	0.5	−0.12
3	$Cu_s \rightarrow Cu^+_{aq} + e^-$	1.50×10^{-2} (1/s)	0.5	−0.12
4	$Cu_s \rightarrow Cu_s$ (surface diffusion)			
5	$Cu^+_{aq} + Cl^-_{aq} \rightarrow CuCl_{ads}$	5.0×10^6 (L^2/mol^2 s)		
6	$CuCl_{ads} \rightarrow Cu^+_{aq} + Cl^-_{aq}$	1.0×10^1 (1/s)		
7	$CuCl_{ads} + e^- \rightarrow Cu_s + Cl^-_{aq}$	1.0×10^{-2} (1/s)	0.5	−0.12
8	$CuCl_{ads} + PEG_{aq} \rightarrow CuClPEG_{ads}$	1.103×10^5 (L/mol s)		
9	$CuClPEG_{ads} \rightarrow CuCl_{ads} + PEG_{aq}$	7.0×10^{-1} (1/s)		
10	$SPS_{aq} + 2e^- \rightarrow 2thiolate^-_{aq}$	1 (L/mol s)	0.5	−0.4
11	$Cu^+_{aq} + MPS_{aq} \rightarrow Cu(I)thiolate_{ads} + H^+_{aq}$	1.0×10^6 (L^2/mol^2 s)		
12	$Cu(I)thiolate_{ads} + H^+_{aq} \rightarrow Cu^+_{aq} + MPS_{aq}$	1.0×10^{-1} (L/mol s)		
13	$Cu^+_{aq} + Cu(I)thiolate_{ads} + e^- \rightarrow Cu(I)thiolate_{ads} + Cu$	2.11×10^1 (L/mol s)	0.5	−0.12
14	$Cu(I)thiolate_{ads} + HIT_{aq} \rightarrow Cu(I)HIT_{ads} + MPS_{aq}$	3.0×10^6 (L/mol s)		
15	$Cu(I)HIT(I)_{ads} + H^+_{aq} + e^- \rightarrow HIT_{aq} + Cu$	1.5×10^5 (L/mol s)	0.5	−0.12

Homogeneous chemical reactions in bulk electrolyte.

j	Homogeneous reactions	Equilibrium constant K_j	Ref.
16	$MPS_{aq} \leftrightarrow H^+_{aq} + thiolate^-_{aq}$	10^{-7} M	49
17	$H_2SO_{4,aq} \leftrightarrow HSO^-_{4,aq} + H^-_{aq}$	Complete dissociation	—
18	$HSO^-_{4,aq} \leftrightarrow SO^{2-}_{4,aq} + H^+_{aq}$	10^{-2} M	49

Surface diffusion

j	Surface diffusion	Surface diffusion coefficient (cm^2/s)	Broken energy barrier (kJ/mol)	Step energy barrier (kJ/mol)	Ref.
4	$Cu_s \rightarrow Cu_s$	2×10^{-7}	−27	−27	50

b. Solution species and their physical properties.

i	Charge number z_i	Bulk diffusion coefficient D_i ($\times 10^5$ cm^2/s)	Ref.
Cu^{2+}	2	0.714	49
Cu^+	1	1	—
Cl^-	1	2.032	49
PEG	0	0.07	8, Error! Book mark not defined.
SPS	0	1	8, Error! Book mark not defined.
MPS	0	1	—
$Thiolate^-$	1	1	—
HIT	0	1	—
H^+	1	9.311	49
HSO^-_4	1	1.331	49
SO^{2-}_4	2	1.065	49
H_2SO_4	0	1	—

[a] In this table, the subscript aq denotes an aqueous species, ads denotes surface adsorbed species, and s denotes solid Cu on a lattice site. CuClPEG represents the complex Cl–Cu(I)-PEG, Cu(I) thiolate represents the complex $Cu(I)[-S(CH_2)_3SO_3H]$. Because of unclear solution chemistry of HIT, Cu(I) HIT is used to represent the complex formed between Cu(I) and HIT.

reactions, where the hypothetical additive mechanism was represented by a set of ordinary differential equations for all of the reactions in Table Ia.

The electron-transfer coefficient α_j was set at 0.5 for all of the electrochemical reactions listed in Table Ia. The equilibrium potentials for Reactions 1 and 3 were set as −0.50 and −0.12 V, respectively.[36] Due to limited information, the equilibrium potentials for other Cu(I) complex reduction reactions (Reactions 3, 7, 13, and 15) were also set as −0.12 V. Unknown kinetic rate parameters were then adjusted so that the simulated current responses roughly matched the results from RDE experiments. Initial estimates for rate constants k_1 and k_2 were obtained by fitting the model to the transient current responses measured in RDE experiments. The rate constant k_3 was chosen as similar to the value for k_2, since copper dissolution (Reaction 3) is not significant in the cathodic region under study. Rate constants k_5 and k_6 were set so that the CuCl coverage stays in a moderate range under normal plating potentials when no PEG is added in the plating solution; the desorption rate constant k_7 was then set so that CuCl remains on the surface. Rate constants k_8 and k_9 were adjusted to ensure that CuClPEG coverage at steady state was about 95% if no SPS is added, which is consistent with experimental observations.[37] The equilibrium potential for the SPS/thiolate couple was set at −0.4 V, which is sufficient to

convert most of the SPS that reaches the surface to thiolate if Cu-ClPEG does not block the bare copper surface sites. Rate constants k_{11}–k_{13} were then adjusted to give the catalytic acceleration effect when SPS is added. Rate constants k_{14} and k_{15} were set to high values so that one HIT molecule can remove many accelerator Cu(I) thiolate molecules.

Effect of local area change.— Moffat et al.[38,39] proposed the curvature-enhanced-accelerator coverage (CEAC) model to account for the local area change during the trench infill by copper electrodeposition. Here we consider a material balance on the adsorbed catalyst [Cu(I) thiolate], whose surface coverage changes with the change in local surface area: the real area of metal/electrolyte interface associated with each KMC code varies with time, so the surface concentration of catalyst is corrected accordingly at each iteration.

If an infinitesimal two-dimensional (2D) curve γ is moving in the direction normal to itself with a speed function v, then the change of arc length can be calculated from the curvature κ

$$\frac{l^{t+1}}{l^t} = 1 + \kappa v \qquad [16]$$

where l^t and l^{t+1} are the values of arc length at time t and $t + 1$, respectively. In general, for a smooth 2D curve with arc length s, the change of arc length becomes

$$\frac{l^{t+1}}{l^t} = \frac{\int_\gamma [1 + \kappa(s)v(s)]ds}{\int_\gamma ds} \qquad [17]$$

The corresponding increment of the surface coverage of the segregated catalytic species over the time interval in the simulation code is computed by

$$\Delta\theta^{t+1}_{\text{catalyst}} = \theta^{t+1}_{\text{catalyst}} - \theta^{t}_{\text{catalyst}} = \theta^{t}_{\text{catalyst}}\left(\frac{l^{t+1}}{l^t} - 1\right) \qquad [18]$$

Hence, if the surface is convex, then κ is greater than zero, $l^{t+1}/l^t > 1$, and $\Delta\theta^{t+1}_{\text{catalyst}} > 0$; if the surface is concave, then κ is less than zero, $l^{t+1}/l^t < 1$, and $\Delta\theta^{t+1}_{\text{catalyst}} < 0$.

The area change by Eq. 17 is calculated from the local curvature by the level-set code and sent to the KMC codes at the different trench surface locations, while the KMC codes calculate the changes of the catalyst surface coverage at different locations with Eq. 18. Since the lattice size of each KMC simulation is fixed, an increase of θ_{catalyst} is implemented in the code by inserting mesoparticles of the catalyst onto the surface and releasing absorbed CuClPEG back into the solution via Reaction 9. When θ_{catalyst} reaches 1, the excessive catalyst on the surface due to the further surface area decrease is also released into the solution. In this way the mass of all chemical species during the simulation is conserved. A decrease of θ_{catalyst} is implemented in the opposite way.

Results and Discussion

Verification simulations.— The KMC code was validated by comparison with simulation and theoretical results for various limiting cases of behavior. Details of the code validation are described in a previous publication.[24] The validation studies included comparisons of the (*i*) root-mean-square distance of travel for single atoms on a flat surface with its theoretical value as a function of time, (*ii*) surface coverages for large values of the surface diffusion coefficient in the KMC code with theoretical values obtained for infinite diffusion coefficient, and (*iii*) the surface roughness as a function of length scale for varying mesoparticle sizes. In addition,[28] comparisons were carried out of the concentration and potential variation in a 1D diffusion/migration layer with results reported previously[28] by Newman. The following therefore focuses on the validation of the continuum code.

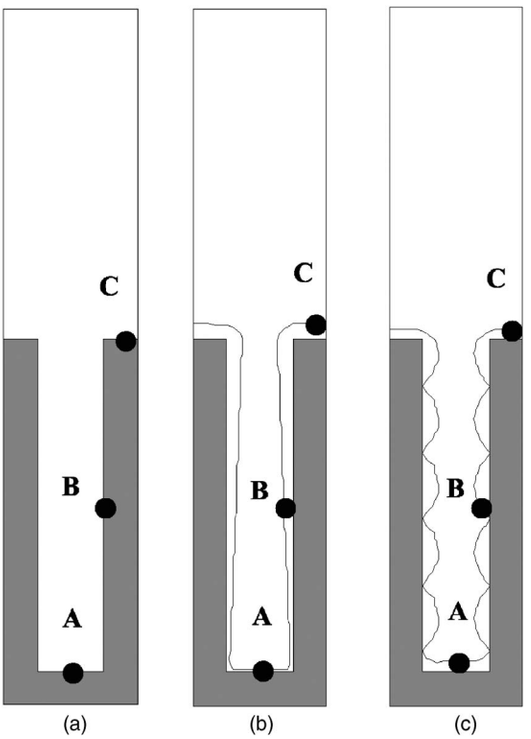

Figure 5. The initial configuration of different metal/electrolyte interfaces used for the continuum code validation by comparison with results obtained with commercial software (COMSOL Multiphysics). The interfaces are when (a) no copper has been deposited, (b) copper has been deposited for 0.4 s with fluxes given by Eq. 24, and (c) copper has been deposited for 0.4 s with fluxes given by Eq. 25. Points A, B, and C correspond to points where comparisons were made (see Table II).

2D trench in-fill.— To validate the 2D continuum code and test its capability of handling different metal/electrolyte interfaces, its results were compared with COMSOL Multiphysics, a commercial software package for the modeling and simulation of the physical processes based on the finite-element method.[28] The electrolyte consisted of three ionic species (Cu^{2+}, H^+, HSO_4^-) which move by diffusion and migration. Three geometric configurations were examined by imposing "dummy fluxes" as boundary conditions along the sidewall; the dummy fluxes corresponded to a linear variation in local deposition rate. Three cases for the initial metal/electrolyte profile were chosen as shown schematically in Fig. 5: (a) the initial trench configuration, (b) a partially filled trench with a linear variation of deposition thickness along the sidewall which would correspond to case (a) after 0.4 s, and (c) a periodic set of sidewall bumps. The dimensions of the 2D simulation domain used for these validation studies (see Fig. 1) were

$$w_t = 0.15\ \mu\text{m}, \quad h_t = 0.75\ \mu\text{m}, \quad h_{bl} = 0.75\ \mu\text{m}$$

The dummy sidewall fluxes for cases (a) and (b) were

$$J_{Cu^{2+}} = 6.0 \times 10^{-4} + 5.8 \times 10^{-3}y$$

$$J_{H^+} = J_{HSO_4^-} = 0 \qquad [19]$$

where (x,y) is the point on the interface and $y \in [0,h_t]$. The dummy sidewall flux for case (c) was

$$J_{Cu^{2+}} = 6.0 \times 10^{-3}|\cos(6.7\pi y)|$$

Table II. Comparison of FEMLAB results and continuum code results with metal/electrolyte interfaces in Fig. 5.

		Concentration of Cu^{2+} (M)		Potential ($\times 10^3$ V)	
Figure 7	Node	FEMLAB	Continuum	FEMLAB	Continuum
a	A	0.28859	0.28857	−0.4905	−0.4916
	B	0.28941	0.28939	−0.4552	−0.4562
	C	0.29362	0.29362	−0.2735	−0.2737
b	A	0.28524	0.28523	−0.6356	−0.6356
	B	0.28620	0.28619	−0.5939	−0.5940
	C	0.29338	0.29338	−0.2841	−0.2842
c	A	0.27804	0.27778	−0.9646	−0.9746
	B	0.28093	0.28067	−0.8330	−0.8430
	C	0.29229	0.29199	−0.3343	−0.3468

$$J_{H^+} = J_{HSO_4^-} = 0 \quad [20]$$

The COMSOL code used the default mesh parameters in COSMOL Multiphysics, and the continuum code chose the mesh size to be 0.015 μm. With the initial metal/electrolyte interface and the dummy fluxes, the electrochemical system was solved from $t = 0$ to 0.5 s. Table II shows the Cu^{2+} concentration and potential produced by the two methods at points A, B, and C on the interface. It may be seen that the agreement between the two methods of calculation was good to the fourth significant figure. Although the dimensions used here are slightly different from those used for the additional results reported below (see Table III), the results in Table III provide a clear indication of the numerical accuracy of the coupled FV and level-set code.

Multiscale simulation of copper electrodeposition in trench.— This section illustrates several kinds of results that may be obtained with the multiscale code. Due to uncertainty in the reaction mechanism, as well as the associated system parameters, the discussion here is focused on the simulation method. All numerical results presented below were obtained with 11 processors on a Xeon Linux Cluster located at the National Center for Supercomputing Applications (NCSA). The Intel Xeon processor has a clock speed of 3.2 GHz, with a 512 kB L2 data cache, and a 1 MB L3 data cache. The codes were written in FORTRAN 90 and compiled with the "-O2" option.

Five test simulations were performed with ten KMC nodes deployed along the trench as illustrated in Fig. 3. The electrolyte composition and other parameters used in the simulation are documented in Table III. The KMC simulations were run on a 50×50 lattice and the mesoparticle size was set to be 0.50 nm. The coarse grid mesh size in the FV code was 0.02 μm, and the fine grid mesh size in the level-set code was 2.5 nm. It was found that the run time for all three codes varied with the number of mesh points as N^2. A small external time step (0.002 s) was used for exchanging boundary conditions between the continuum code and KMC codes in order to ensure an accurate mass balance calculation for low concentration species at the metal-solution interface. It took about 20 hours to complete one simulation, about 80% of which was spent in the FV code and 20% in the KMC code.

The purpose of these test simulations is to demonstrate that the approach is feasible and to illustrate the type of numerical results that can be obtained. It is emphasized that the values for the initial parameters used in these test simulations are uncertain, and that it would be inappropriate to draw conclusions about the reaction system at this time. Figure 6 shows shape evolution sequences during trench fill for the five test simulations, where each line marks the position of the copper surface for every 5 s. The electrolyte associated with Fig. 6a contains all four additives in concentrations for which "superfilling" is known to occur. It may be seen that near the beginning of the simulation, the copper growth rates are nearly uniform everywhere. After a few seconds, copper reduction at the top of the trench becomes suppressed while the reduction of copper at the bottom of the trench is accelerated. Because of a significant differential deposition rate between the top and bottom, the bottom of the trench fills rapidly. Once the trench is completely filled with copper, a bump forms and then gradually disappears as additional copper is deposited. These results demonstrate that complex macroscopic shape-evolution events can be simulated over extended peri-

Table III. Parameters used in the multiscale trench infill simulation.

a. Bulk concentrations

Figure	$CuSO_4$ (M)	H_2SO_4 (M)	HCl (M)	PEG (M)	SPS (M)	HIT (M)
8a	0.3	1.27	1.55×10^{-3}	8.8×10^{-5}	1.7×10^{-5}	7.0×10^{-7}
8b	0.3	1.27	1.55×10^{-3}	8.8×10^{-5}	—	—
8c	0.3	1.27	1.55×10^{-3}	8.8×10^{-5}	2.8×10^{-4}	—
8d	0.3	1.27	—	—	1.7×10^{-5}	—
8e	0.3	1.27	1.55×10^{-3}	8.8×10^{-5}	1.7×10^{-5}	—

b. Parameters used in simulation

Parameter	Value
i_{wafer}	0.042 A/cm^2
w_t	0.2 μm
w_d	0.3 μm
h_t	1 μm
h_{bl}	50 μm
l_{KMC}	0.0005 μm
N_{KMC}	50
T	2988 K
External time step	0.002 s

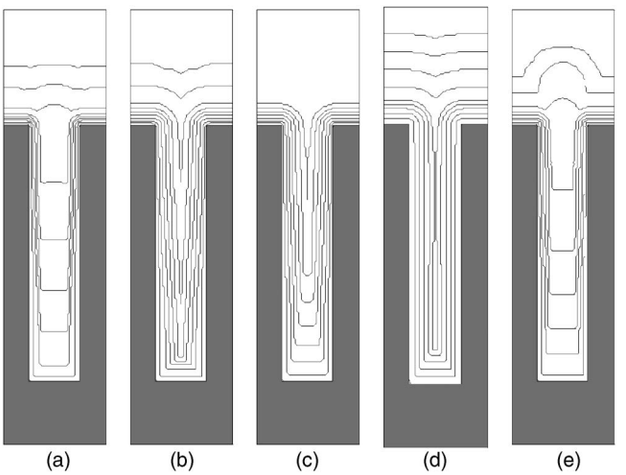

Figure 6. Simulated shape evolution of trench fill under various conditions. (See Table IIIa for the corresponding electrolyte composition, and Tables I and IIIb for the reaction chemistry and system parameters.)

ods of time with simultaneous simulation of microscopic roughness evolution associated with nearly molecular scale events at the surface.

For the case shown in Fig. 6a, the concentration distributions for several species within the trench are provided in Fig. 7 as a function of time. (The axis marked "KMC Positions" indicates the position along the surface that corresponds to each of the KMC nodes as illustrated in Fig. 3, with 1 being at the top and 10 at the bottom of the trench.) It may be seen that the surface species in the KMC code (e.g., Cu, CuClPEG, CuCl) show stochastic noise in the concentration distributions. Because the KMC code passes the flux to the continuum code (see Fig. 4), the noise is also seen in the time variation of the electrolyte concentration profiles. However, for the species in the continuum model, the concentration variation between the top and bottom of the trench is essentially negligible. It is also seen that there is a delay in the onset of MPS generation by Reaction 16, as well as in the increase of Cu(I) thiolate coverage at the bottom of the trench. Once the trench is filled, the local copper reduction rate remains high and a bump begins to form on top of the trench. However, as the surface area starts to increase, the coverage of Cu(I) thiolate is reduced in accordance with conservation of mass on the surface, as well as interactions with PEG. As the Cu(I) thiolate coverage decreases to nearly zero, the growth of the bump ceases. The foregoing test simulations demonstrate various kinds of interactions between species in the mechanism associated with transport and reaction within the trench during deposition.

In the proposed additive mechanism, the Cu^{+}_{aq} species is an "active intermediate" which is present at dilute levels as determined by its generation (by Reaction 1) and consumption (by Reactions 2, 5, 11, 13). All of the consumption reactions involve surface species in the KMC codes, with the consequence that the Cu^{+}_{aq} flux values passed to the continuum code from the KMC codes (see Fig. 4) can be noisy. It was found that numerical instabilities occurred in the continuum code, so a filter was introduced between the KMC code and the continuum code to overcome the problem.[40,41]

Shape evolution results presented in Fig. 6b show the nearly conformal growth of copper inside the trench in the absence of SPS and HIT. The results seen in Fig. 6c (with high SPS concentration) indicate that copper grows faster near the trench opening, which leads to sidewall closure, which is typically associated with formation of small voids inside the trench. Figure 6d illustrates that shape evolution with only SPS in the solution leads to conformal growth due to the lack of suppression on top of the trench. Figure 6e provides results obtained in the absence of leveler HIT, which show that a large copper bump is formed after the trench is completely filled.

Conclusions

A multiscale simulation model was developed which takes advantage of both the ability of KMC methods for describing complex chemical mechanisms on surfaces, and the efficiency of continuum methods for simulating transport and homogeneous reactions in the electrolyte. The model was used to simulate shape evolution during copper electrodeposition in submicrometer trenches according to a hypothetical reaction mechanism involving additives.

It was found that a coarse-grained (2 + 1)D KMC code enabled the simulation of surface roughness evolution at the near molecular scale for a system governed by complex chemical and electrochemical surface reactions. A multisite mesoparticle approach was introduced to account for large molecules (such as PEG). Demonstration calculations were carried out with coarse-grained KMC mesoparticles of 0.5 nm for 50×50 sites; in general, the selection of mesoparticle size would be made according to experimental as well as numerical constraints.

A novel multiscale simulation model that dynamically coupled a MB continuum code with a "necklace" of KMC patches along the surface was developed in this study. It was found that the FV method, which guarantees conservation of mass, was more stable than the finite difference method. The LSM was used to track to movement of the metal/electrolyte interface. The MB continuum code dynamically solved the mass-transfer equations in electrochemical systems with diffusion, migration, and homogeneous chemical reactions with a moving metal/electrolyte interface. A hypothesis for a four-additive mechanism (Table I) was proposed for use in demonstration calculations. The effect of local area change during trench in-fill was considered based on the material balance of absorbed catalytic species on the metal/electrolyte surface.

It was found that the use of a coarse FV mesh with a fine level-set mesh improves code efficiency and provides accurate interface tracking. It was found that most of the central processing unit time was spent on the MB code (25,000 time steps, each of which involved about 1000 KMC steps). For such cases, enhancements of the KMC code, such as increasing the number of surface sites to improve shape resolution, could be made at relatively low additional computational cost. Strategies that result in fewer MB time steps would significantly reduce simulation time.

Two verification tests were carried out for the continuum code for a simple electrolyte containing three species. In the first test, results obtained for a simple 1D configuration were used to compare the simulation algorithm with a well-established numerical procedure. In the second test, results for 2D computations with a more complex geometrical configuration were compared with those obtained with a well-established commercial code (Table II). In each case, agreement was shown to the third significant figure.

Simulations of shape evolution during trench infill were carried out with initial qualitative estimates of the system parameters made with use of literature data, current–voltage experiments, and intuition. It was shown (Fig. 6) that complex macroscopic shape evolution can be tracked over extended periods of time while simultaneously simulating microscopic roughness evolution associated with nearly molecular scale events at the surface.

The simulations reported here illustrate new capabilities that are not provided by previous algorithms. Predictions were obtained of the concentration distributions as a function of time and distance (Fig. 7) for the 14 solute and adsorbed species associated with the reaction mechanism. Such results demonstrate treatment of various kinds of interactions between species in the mechanism associated with transport and reaction during deposition and their influence on morphological outcomes. It was found that Cu^{+} introduced noise and numerical instabilities which were overcome with use of a filter.

The multiscale approach provides several capabilities that are unique. The incorporation of surface-chemistry phenomena in a KMC code coupled with transient diffusion-migration reaction in a MB code makes possible the detailed analysis of experimental atomic force microscopy images of roughness evolution. The multiscale code provides a more general form which can be extended to

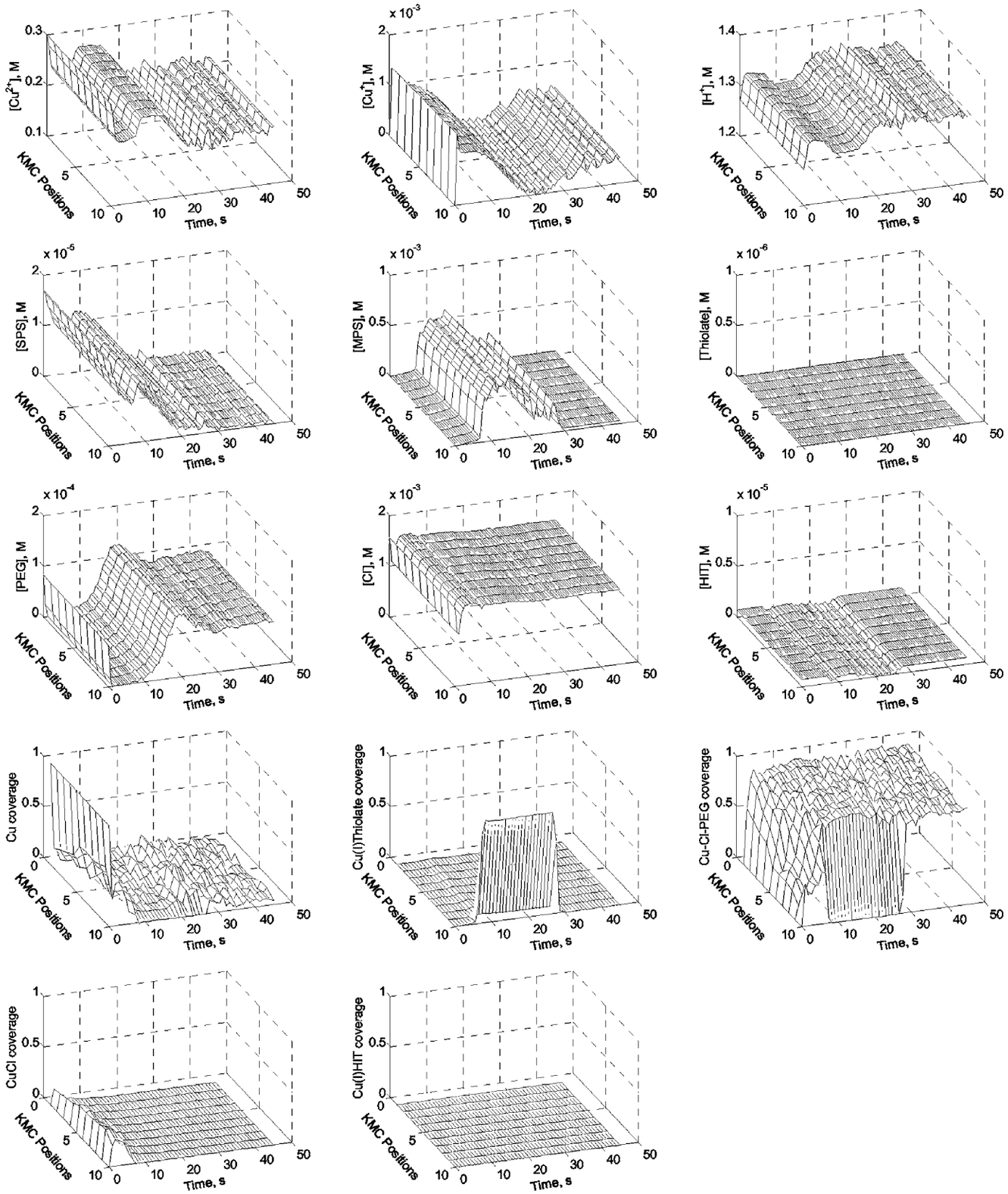

Figure 7. Time and position dependence of the concentrations of solution species and the coverages of surface species at the metal/electrolyte interface. The numbers on the "KMC positions" axis indicate the KMC domain position with "1" corresponding to the mouth of the trench and "10" corresponding to the bottom of the trench (see Fig. 3).

other physical systems. In addition, the method may be extended to the consideration of nonlinear kinetics due to spatial inhomogeneities and lateral adsorbate–adsorbate interactions on surfaces[42] which cannot be simulated using the continuum method. For ex-

ample, transient additive interactions were found to be important for modeling of the bottom-up fill process in a recent study by Akolkar et al.[43] The code can be simplified when applied to a specific problem. For example, some terms in the dilute solution model may be deleted if their effects are negligible, and the KMC code may be replaced with a system of ordinary differential equations if surface reactions are essentially first order with regard to surface species.

Acknowledgments

Funding for this work was provided by the National Science Foundation under grants CTS-0135621 and CTS-0438356 and via the National Computational Science Alliance (NCSA) under grant ACI 96-19019 and computing resource allocation NRAC MCA-01S022. Any opinions, findings, and conclusions or recommendations expressed in this material are those of the authors and do not necessarily reflect the views of the National Science Foundation. Support was also received from an IBM Faculty Partnership and an IBM Predoctoral Fellowship Award for F. Xue. The authors acknowledge with appreciation the assistance of J. Alameda (NCSA, University of Illinois, Urbana) and of H. Deligianni, P. Vereecken, and P. Andricacos (IBM, T. J. Watson Research Center, Yorktown Heights, NY).

The University of Illinois at Urbana-Champaign assisted in meeting the publication costs of this article.

Appendix A
KMC Algorithm

The KMC algorithm employed here is similar to that described by Levi and Kotrla[44] and Battaile et al.[45] used for simulations of crystal growth. Details are available in Ref. 46.

1. Choose a random number, U_1, from a uniform distribution in the range (0,1).
2. Select the transition event from the list by selecting the first index s for which $\Sigma_{j=1}^{s} n_j r_j \geq U_1$.
3. Choose the lattice site from n_s randomly by generating another random number U_2, uniformly distributed in (0,1).
4. Implement the transition event s at the chosen site with rate r_s.
5. Update all r_j that changed as a result of step 3.
6. Advance the time in the simulations according to Eq. 2. Return to step 1.

In more detail, the rates are binned by type in order to speed up the simulations. The computational expense is reduced by using structured lists when coding the KMC algorithm:

1. Information about each rate is stored in a matrix. The site number is unique for each site on the surface. Periodic boundary conditions are used in the x and y directions.
2. At the beginning of the simulation, all of the rates for all possible moves are tabulated and cataloged. These rates are only recalculated when a move occurs at a site or one of its eight nearest neighbors.
3. All of the possible rates in the system are binned to create a list that is used to select which events occur.
4. The rates are normalized and a uniformly distributed random number U_1 is generated on the interval (0,1).
5. Once the random number is generated, the appropriate event is selected from the list.
6. Next, an instance of that event is selected randomly from the bin for that rate by generating another uniformly distributed random number U_2 in (0,1) and the action is executed.
7. The appropriate neighbor rates are updated in the site list depending on the action that is taken.
8. The time in the system is updated and the process is repeated.

This (2 + 1)D KMC model uses the rate-based approach which formulates all actions in terms of rates and checks a single site per Monte Carlo time step. Null events are eliminated in this approach. There is a single Monte Carlo time step in the simulation that is a function of the species and their associated rates. It is possible to simulate the effect of low concentration additives and steric effects with this KMC formulation.

Appendix B
Constant Current Copper Deposition

Industrial practice for on-chip interconnect fabrication employs controlled current conditions, whereas virtually all modern scientific studies on electrodeposition are carried out under controlled potential conditions. Therefore, for the application at hand, a constant-current model was used, which required a controller because the external input to the KMC code is the applied potential. The applied potential (E_{appl}) in the copper electrodeposition is the sum of the equilibrium cell potential (E^o), the potential drop between the reference electrode and the working electrode due to solution resistance (E_{IR}), and the kinetic overpotential (η)

$$E_{appl} = E^o + E_{IR} + \eta \qquad [B\text{-}1]$$

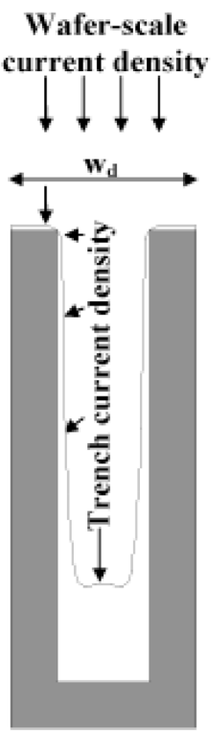

Figure B-1. The projection of the wafer-scale current density into the trench current density. It is calculated by the ratio of w_d to the total length of the copper-solution interface, in a 2D view.

In order to simulate copper electrodeposition under constant current operating conditions, the applied potential must vary with time. Here the approach of Rusli et al.[47,48] was used to design a gain-scheduled feedforward-feedback controller to dynamically alter the applied potential values to the KMC codes and track the current consumption. The controller was designed based on a low-order model that captured the most essential input-output behavior of the process with the manipulated input being the applied potential and the process output being the current density. The low-order model is in the form of

$$i = a_1 e^{-a_2 \eta} C^s \qquad [B\text{-}2]$$

where i is the current density, η is the applied potential, C^s concentration of Cu^{2+} at the surface, and a_1, a_2 are the parameters to fit. The feedback controller was designed to give the first-order closed-loop response

$$\frac{i}{i_r} = GG_c(1 + GG_c)^{-1} = \frac{\beta}{1 - (1 - \beta)z^{-1}} \qquad [B\text{-}3]$$

where $\beta \in (0,1)$, i_r is the set point of the current density, z^{-1} is a delay operator, and G and G_c are the input-output operators for the plant and the controller, respectively. Equation B-3 was rearranged to give the feedback controller

$$G_c = \frac{\beta}{K(1 - z^{-1})} \qquad [B\text{-}4]$$

The feedforward element was derived from Eq. B-2

$$\eta = -\frac{1}{a_2} \ln\left(\frac{i}{a_1 C^s}\right) \qquad [B\text{-}5]$$

In the simulation of the copper deposition process, the wafer-scale current density that is perpendicular to the wafer surface needs to be constant (see Fig. B-1.). The wafer-scale current density was converted to the average local current density inside the trench which was used as the set point to the controller. The relation between the average local current density inside trench and the wafer-scale current density is given by

$$\text{average local current density inside trench} = \frac{\text{vertical projection area} \times \text{wafer-scale current density}}{\text{total copper-solution interface area}} \qquad [B\text{-}6]$$

where the vertical projection area and the total copper-solution interface area are calculated from the LSM code.

List of Symbols

A_i	production rate of a species i due to homogeneous reactions in the bulk solution, M/s
$\tilde{A}_i$	cell averaged production rate of a species i due to homogeneous reactions in the bulk solution, M/s
C_i	concentration of species i, M
$\tilde{C}_i$	cell averaged concentration of species i, M
C_i^∞	bulk concentration of species i, M
C^s	concentration of species at the surface, M
D_i	diffusion coefficient of species i, cm^2/s
E_j^0	equilibrium potential of reaction j, V
E_{IR}	solution resistance, V
E_{appl}	applied potential, V
F	Faraday's constant, 9.65×10^4 C/equiv
G	input-output operator for process
G_c	input-output operator for controller
h_t	depth of the trench, μm
h_{bl}	height of the external diffusion layer above the trench, μm
i_r	set point of current density, A/cm^2
i_{wafer}	current per wafer surface area (wafer scale current density), A/cm^2
J_i	flux of species i, mol/cm^2 s
k_j	reaction rate constant for reaction j in Table Ia
K_j	equilibrium constant of homogeneous reaction j in bulk solution, see Table Ia
K_p	process gain
l_{KMC}	edge length of each square mesoparticle simulated in the KMC code, μm
m	total number of surface sites that a multisite mesoparticle should occupy
M	number of transition events
$\bar{\mathbf{n}}$	normal direction of the metal/electrolyte interface
n_{KMC}	number of the mesoparticles simulated in each of the KMC code
n_j	number of lattice sites out of N that are capable of undergoing a transition event with rate r_j
N	number of lattice sites in kinetic Monte Carlo code
$\bar{\mathbf{N}}_i$	flux of species i, mol/cm^2
r_j	rate of transition event j
R	universal gas constant, 8.314 J/mol K
T	absolute temperature, 298 K
u_i	mobility of species i, D_i/RT, cm^2 mol/J s
U	random number with uniform distribution, $U \in (0,1)$
v	magnitude of velocity on the interface
v_{ext}	extension of velocity
V	cell volume in the FV method
w_t	width of the bottom of the trench, μm
w_d	width of the total area of a single trench occupies on the wafer, μm
W_j	probability of transition event j occurring
y	a distance, $0 < y < h_t$, measured up from the bottom of the initial trench, μm
z_i	charge number of species i

Greek

α_j	transfer coefficient of reaction j
β	parameter in controller
ϕ	level-set function
Φ	potential in solution, V
Φ^∞	potential in bulk solution at the outer edge of the mass-transfer boundary layer, V
η	overpotential, V
$\theta_{catalyst}$	surface coverage of catalyst
τ	time step in kinetic Monte Carlo algorithm, s

References

1. R. Alkire and M. Verhoff, *Chem. Eng. Sci.*, **49**, 4085 (1995).
2. R. Alkire and M. Verhoff, *Electrochim. Acta*, **43**, 2733 (1998).
3. R. C. Alkire and R. D. Braatz, *AIChE J.*, **50**, 2000 (2004).
4. R. Alkire, *J. Electroanal. Chem.*, **559**, 3 (2003).
5. P. C. Andricacos, C. Uzoh, J. Dukovic, J. Horkanes, and H. Deligianni, *IBM J. Res. Dev.*, **42**, 567 (1998).
6. Y. Cao, P. Taephaisitphongse, R. Chalupa, and A. C. West, *J. Electrochem. Soc.*, **148**, C466 (2001).
7. Y. H. Im, M. O. Bloomfield, S. Sen, and T. S. Cale, *Electrochem. Solid-State Lett.*, **6**, C42 (2003).
8. M. Georgiadou, D. Veyret, R. L. Sani, and R. C. Alkire, *J. Electrochem. Soc.*, **148**, C54 (2001).
9. M. Georgiadou and D. Veyret, *J. Electrochem. Soc.*, **149**, C324 (2002).
10. D. Wheeler, D. Josell, and T. P. Moffat, *J. Electrochem. Soc.*, **150**, C302 (2003).
11. T. J. Pricer, M. J. Kusher, and R. C. Alkire, *J. Electrochem. Soc.*, **149**, C396 (2002).
12. T. J. Pricer, M. J. Kusher, and R. C. Alkire, *J. Electrochem. Soc.*, **149**, C406 (2002).
13. T. S. Cale, M. O. Bloomfield, D. F. Richards, K. E. Jansen, and M. K. Gobbert, *Comput. Mater. Sci.*, **23**, 3 (2002).
14. R. Lam and D. G. Vlachos, *Phys. Rev. B*, **64**, 035401 (2001).
15. U. Hansen, S. Rodgers, and K. F. Jensen, *Phys. Rev. B*, **62**, 2869 (2000).
16. A. B. Bortz, M. H. Kalos, and J. L. Lebowitz, *J. Comput. Phys.*, **17**, 10 (1975).
17. Y. G. Yang, R. A. Johnson, and H. N. G. Wadley, *Surf. Sci.*, **499**, 141 (2002).
18. G. Henkelman and H. Jónsson, *J. Chem. Phys.*, **115**, 9657 (2001).
19. J. Lu and M. J. Kushner, *J. Vac. Sci. Technol. A*, **19**, 2652 (2001).
20. G. A. Bird, *Molecular Gas Dynamics and the Direct Simulation of Gas Flows*, Clarendon Press, Oxford (1994).
21. C. K. Birdsall and A. B. Langdon, *Plasma Physics via Computer Simulation*, McGraw-Hill, New York (1985).
22. M. A. Katsoulakis, A. J. Majda, and D. G. Vlachos, *J. Comput. Phys.*, **186**, 250 (2003).
23. R. D. Braatz, R. C. Alkire, E. Seebauer, E. Rusli, R. Gunawan, T. O. Drews, X. Li, and Y. He, *J. Process Control*, **16**, 193 (2006).
24. T. O. Drews, R. D. Braatz, and R. C. Alkire, *Int. J. Multiscale Comp. Eng.*, **2**, 313 (2004).
25. J. S. Newman, *Electrochemical Systems*, p. 241, Prentice-Hall, Englewood Cliffs, NJ (1991).
26. K. M. Takahashi and M. E. Gross, *J. Electrochem. Soc.*, **146**, 4499 (1999).
27. W. E. Schiesser, *The Numerical Method of Lines: Integration of Partial Differential Equations*, Academic Press, New York (1991).
28. X. Li., M.S. Thesis, University of Illinois at Urbana-Champaign, Urbana, IL (2004).
29. S. Li and L. R. Petzold, *J. Comput. Appl. Math.*, **125**, 131 (2000).
30. J. A. Sethian, *Level Set Methods and Fast Marching Methods*, Cambridge University Press, Cambridge, UK (1999).
31. X. H. Li, Ph.D. Thesis, University of Illinois at Urbana-Champaign (2007).
32. C. W. Gear, J. Li, and I. G. Kevrekidis, *Phys. Lett. A*, **316**, 190 (2003).
33. W. Gropp, E. Lusk and A. Skjellum, *Using MPI*, 2nd ed., MIT Press, Cumberland, RI (1999).
34. P. M. Vereecken, R. A. Binstead, H. Deligianni, and P. C. Andricacos, *IBM J. Res. Dev.*, **49**, 3 (2005).
35. F. Xue, Ph.D. Thesis, University of Illinois at Urbana-Champaign, Urbana, IL (2006).
36. G. Prentice, *Electrochemical Engineering Principles*, p. 270, Prentice Hall, Englewood Cliffs, NJ (1991).
37. J. J. Kelly and A. C. West, *J. Electrochem. Soc.*, **145**, 3472 (1998).
38. T. P. Moffat, B. Baker, D. Wheeler, J. E. Bonevich, M. Edelstein, D. R. Kelly, L. Gan, G. R. Stafford, P. J. Chen, W. F. Egelhoff, and D. Josell, *J. Electrochem. Soc.*, **149**, C423 (2002).
39. T. P. Moffat, D. Wheeler, M. D. Edelstein, and D. Josell, *IBM J. Res. Dev.*, **49**, 19 (2005).
40. E. Rusli, T. O. Drews, and R. D. Braatz, *Chem. Eng. Sci.*, **59**, 5607 (2004).
41. E. Rusli, Ph.D. Thesis, University of Illinois at Urbana-Champaign, Urbana, IL (2006).
42. J. S. Reese, S. Raimondeau, and D. G. Vlachos, *J. Comput. Phys.*, **173**, 302 (2001).
43. R. Akolkar and U. Landau, *J. Electrochem. Soc.*, **151**, C702 (2004).
44. A. C. Levi and M. J. Kotrla, *J. Phys. Condens. Matter*, **9**, 299 (1994).
45. C. C. Battaile, D. J. Srolovitz, and J. E. Butler, *J. Appl. Phys.*, **82**, 6293 (1997).
46. T. O. Drews, Ph.D. Thesis, University of Illinois at Urbana-Champaign, Urbana, IL (2004).
47. E. Rusli, T. O. Drews, D. L. Ma, R. C. Alkire, and R. D. Braatz, *J. Process Control*, **16**(4), 409 (2006).
48. E. Rusli, M.S. Thesis, University of Illinois at Urbana-Champaign, Urbana, IL (2003).
49. P. Vanysek, in *CRC Handbook of Chemistry and Physics*, 79th ed., D. R. Lide, Editor, CRC Press, Boca Raton, FL (1998).
50. S. Baier, S. Dieluweit, and M. Giesen, *Surf. Sci.*, **502–503**, 463 (2002).